

Ultrafast Optical Response of Carbon Films

Vadim M. Farztdinov* and Sergey A. Kovalenko

*Institut für physikalische und theoretische Chemie der Humboldt-Universität zu Berlin,
D-10117 Berlin, Germany*

Yuri E. Lozovik, Dmitrii V. Lisin, and Yuri A. Matveets

Institute of Spectroscopy, RAS, Troitsk, Moscow Region, 142092 Russia

Tatyana S. Zhuravleva and Victor M. Geskin

Institute of Biochemical Physics, RAS, Moscow, 117334 Russia

Lev M. Zemtsov and Vladimir V. Kozlov

Topchiev Institute of Petrochemical Synthesis, RAS, Moscow, 117912, Russia

Gerd Marowsky

Laser Laboratorium Göttingen e.V., D-37077 Göttingen, Germany

Received: July 13, 1999; In Final Form: October 26, 1999

The ultrafast photoinduced optical response of heat (infrared) treated polyacrylonitrile films (PAN-IR) is studied by the femtosecond pump–supercontinuum probe (PSCP) technique in the probe energy region 1.6–3.2 eV. The samples were excited by pulses with duration of 50 fs and photon energy of $\hbar\omega_{\text{pump}} = 2.34$ eV. Two types of films were used corresponding to 600 and 700 °C heating. The structure of the films was investigated with atomic force microscopy, micro-Raman spectroscopy, and optical absorption spectroscopy. The size of the graphitic clusters was evaluated as ~ 13 Å for the first and > 17 Å for the second sample. The study of the photoinduced response shows that its temporal evolution is characterized by two-stage relaxation with fast and slow relaxation rates. For the first type of film, the spectral dependence of the fast relaxation rate shows nonmonotonic behavior with a maximum at $\hbar\omega_{\text{probe}} \approx 1.95$ eV. The region 1.6–1.95 eV shows photoinduced darkening, while the region 1.95–3.2 eV shows photoinduced bleaching. For the second type of film, only photoinduced bleaching is observed, with the fast relaxation rate increasing monotonically. From the analysis of the transient spectra and relaxation rates, two types of optical transitions are proposed. The first is the normal intramolecular absorption when photoexcited electrons stay within the same cluster. The second one is a charge-transfer transition, when the photoexcited electron is transferred from one cluster to another closest one. For large size clusters, the contribution from these transitions vanishes and only intramolecular excitations survive.

1. Introduction

High carbon solids attract considerable attention because of a wide range of their properties^{1–6} and numerous applications. Thin amorphous carbon films are being used as an overcoat to protect magnetic layers from abrasive action of the reading head.⁷ Crystalline, highly conducting graphite films have a number of technological applications.⁸ Carbon films can be prepared with some properties approaching those of diamond.⁹ The glassy carbon microstructures can be used¹⁰ as components in microelectromechanical systems, microreactors, and other systems in which thermal stability, chemical inertness, engineering surface properties, and electrical conductivity are useful characteristics.

Pyrolysis of organic polymers is the simplest and most common method of obtaining polyconjugated carbon structures. A structural conversion of polymer materials, accompanied by release of volatile products and change of chemical composition, depends on pyrolysis conditions. In an inert atmosphere a

temperature increase of a material that was preliminarily structurized in air results in a rise of the carbon content and in carbonization followed by graphitization processes with formation of ordered carbon structures from a network of hexagonal rings and of graphite-like structures.

The practical use of carbon films stimulates the search for new ways of their synthesis. Recently, a new method of obtaining graphite-like carbon films, through pyrolysis of polyacrylonitrile films under noncoherent IR radiation (PAN-IR films), has been suggested.^{11,12} Such films are stable under atmospheric conditions, show good adhesion to different substrates, and possess conductivity that may vary¹³ from 10^{-11} to 10^2 (Ω cm)⁻¹. The chemical transformations, occurring in PAN films during the initial stage of annealing, are similar to IR-induced and thermal annealing. But the new method allows reduction of the time and the temperature of the treatment compared to the traditional thermal process in high-temperature bakes.

The pyrolyzed PAN-IR films are related to glassy carbon films. The structure of glassy and other amorphous carbons (a-C) has been greatly debated (see, for example, an extensive review of the properties of various amorphous carbons in ref 3) because of the ability of carbon to form both 3-fold (sp^2) sites, as in graphite, and 4-fold (sp^3) sites, as in diamond. A number of measured properties suggests that a-C itself is predominantly sp^2 -bonded. At an sp^2 site, three of the valence electrons are used in σ bonds; the fourth enters a π orbital that lies normal to the σ bonding plane. The σ - σ^* gap is maintained at ~ 5.5 eV. The π states are only weakly bonding, so they lie closest to the Fermi level. They therefore fill the gap between σ - σ^* bands and form the valence and conduction band states in a-C.

Graphite (pure sp^2 bonding) itself has no band gap. The presence of a gap in a material with graphite-like structure signifies that the aromatic character does not extend entirely through the sample. Thus, the sp^2 -bonded domains are true islands, despite the fact⁴ that $\geq 95\%$ of all sites might be sp^2 . The π bonding can be broken at the island edges either by the presence of nitrogen¹⁴ or sp^3 sites. Graphitic sheets of fused benzenoid rings are the most stable configuration for large π clusters. Compact clusters are more stable than other combinations such as rows.⁴

Compact graphitic clusters of ~ 10 Å in size have an energy gap of about 1 eV.⁴ An increase of the size of such a cluster changes its electronic structure and leads to a decrease of the energy gap. It is interesting to trace how the increase of the average cluster size is reflected in the physical properties of such materials.

Here, we present a femtosecond pump–supercontinuum probe (PSCP)¹⁵ study of PAN-IR films prepared under different heat treatment conditions. We monitor the broadband photoinduced optical response and analyze the relaxation in such films. We have also measured the stationary optical absorption and micro-Raman spectra and determined the structure of the film surface by using atomic force microscopy (AFM). We concentrate on the interrelation between the material structure and the optical and relaxational properties of PAN-IR films. The information obtained is important both for the analysis of the nature of strongly excited states in these materials and for the determination of their possible use in optoelectronic devices that need a strong photoinduced response with fast switching.

2. Experimental Technique

The samples were prepared by a new method of pyrolysis.^{11,12} PAN films were obtained by spin-casting a PAN solution in dimethylformamide (DMF) on quartz substrates. The film thickness was controlled by the solution concentration and the spin speed and varied from ~ 0.05 to ~ 0.1 μm . Afterward, the films were subjected to a two-stage heat treatment in an IR annealing chamber for preliminary structurization (200 °C, 5.5 h in air) and high-temperature pyrolysis (600–700 °C, 1 min in Ar atmosphere). The radiation sources were 1000 W pulsed halogen lamps with a radiation intensity maximum in the 0.8–1.2 μm region. Samples were placed in a graphite cassette and mounted in quartz holders between the lamps. Since the samples were in the graphite box, they were protected from exposure to visible radiation of the sources. The intensity of the IR radiation was monitored by film temperature measurement with a Chromel thermocouple placed immediately under the sample.

Two types of film were used here corresponding to pyrolysis at 600 °C (first sample) and at 700 °C (second sample). Before pyrolysis the films had the same thickness; afterward, the

thickness of the second-type film was less than that of the first. The final prepared films were flat, being thinner only near the edges. For the optical measurements only the central, homogeneous parts of the films were used. The films thickness was determined from optical absorption by using an absorption coefficient $\alpha = 29$ μm^{-1} at $\hbar\omega = 4$ eV^{14,16} (see below); the values are ~ 0.07 and ~ 0.06 μm for the first and the second film, respectively.

The content of nitrogen in PAN-IR samples is rather high and is estimated¹² as 12 and 7 wt % in the first and the second-type samples, respectively. Following ref 14 we assume that nitrogen atoms are located mainly on the graphitic cluster edges.

Stationary optical absorption spectra were measured with a standard spectrometer ("Lambda 6", Perkin-Elmer). Micro-Raman spectra were registered by using a microscope, double monochromator, and cooled receiver ("T64000", Jobin Yvon). A 458 nm Ar^+ laser with a spot size less than 2 μm was used as a light source. Spectra were recorded at 0.4–1.5 mW laser power. The film morphology was studied with an atomic force microscope ("Nanoscope III", Digital Instruments) both in the contact and tapping modes.

For studying the ultrafast response of PAN-IR films on a quartz substrate, we employed the PSCP technique described in detail elsewhere.¹⁵ This technique provides high time resolution together with broad spectral coverage. The films were excited with optical pulses of ~ 50 fs duration centered at $\hbar\omega_{\text{pump}} = 2.34$ eV. The pump pulse energy was 0.9–1.1 μJ , focused to a spot with a diameter of 150 μm . The supercontinuum probe, covering the spectral range 1.6–3.2 eV, was dispersed by a polychromator at a resolution of ~ 1.5 nm and registered by a photodiode array with 512 pixels. The pump–probe intensity cross-correlation was ~ 70 fs (full width at half-maximum) in the entire spectral range of probing, providing an effective time resolution of 40 fs. The spot diameter of the probe was of 100 μm . All measurements were performed at room temperature in air. During the experiments, we controlled the optical density of the samples and did not observe any irreversible pump-induced changes.

The temporal evolution of the transient pump–probe spectra $\Delta D(\omega, t)$ was monitored by varying the pump–probe delay τ_D in steps of 7 fs up to a maximum time delay of 4 ps. The transient signal was averaged over eight measurements at a repetition rate of 2 Hz. Because the supercontinuum is chirped, the measured spectra had to be time-corrected. We estimate an accuracy of the time correction as ± 15 fs. To extract the relaxation rates, each of the 512 kinetic traces were fitted by a biexponential function convoluted with the pump–probe cross-correlation. In this way the best approximation $\Delta D_{\text{fit}}(\omega, t)$ to the experimental signal $\Delta D(\omega, t)$ was obtained, as will be discussed in section 3.2.

3. Experimental Results

3.1. AFM Images, Micro-Raman Spectra, and Optical Absorption Spectra. Atomic force microscope (AFM) images of the PAN-IR film surfaces are shown in Figure 1. For optimal resolution, the thinner part near the edges of the films was used. It is seen from Figure 1 that the first-type film is rather inhomogeneous with a large number of pores (black places) with sizes of ~ 0.3 μm and average distance between them of ~ 1.5 μm . The film surface is characterized by strong asperity and consists of plane structural compositions of small size (≤ 100 nm). The second-type film (Figure 1b) is much more homogeneous, the pores being practically absent, and the plane structural compositions range in size to ~ 800 nm. These compositions, as seen in AFM, represent cluster aggregates.

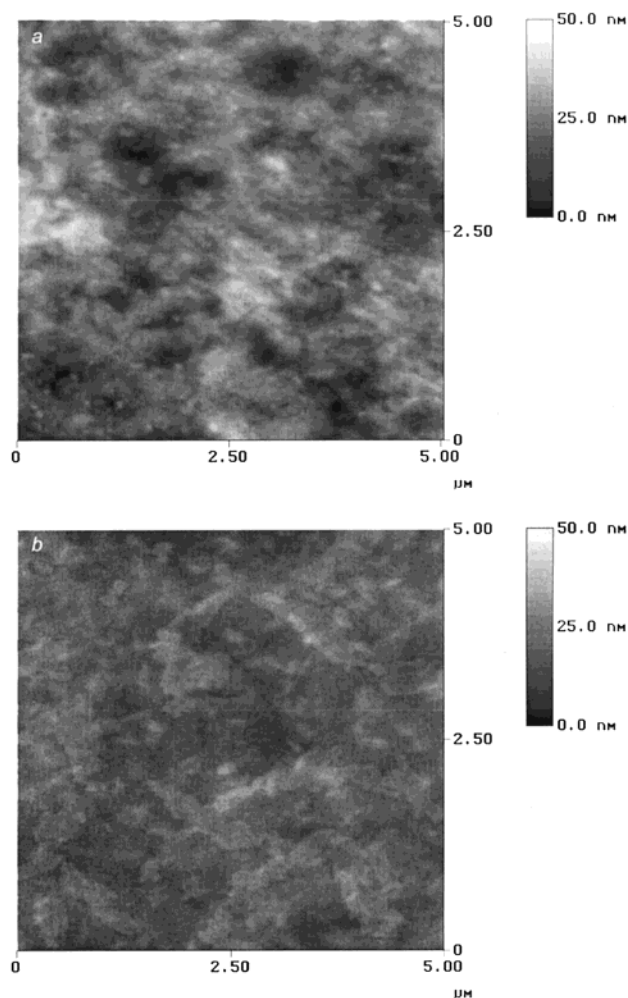


Figure 1. Atomic force microscopy image of the surface of the first sample (a) and of the second sample (b).

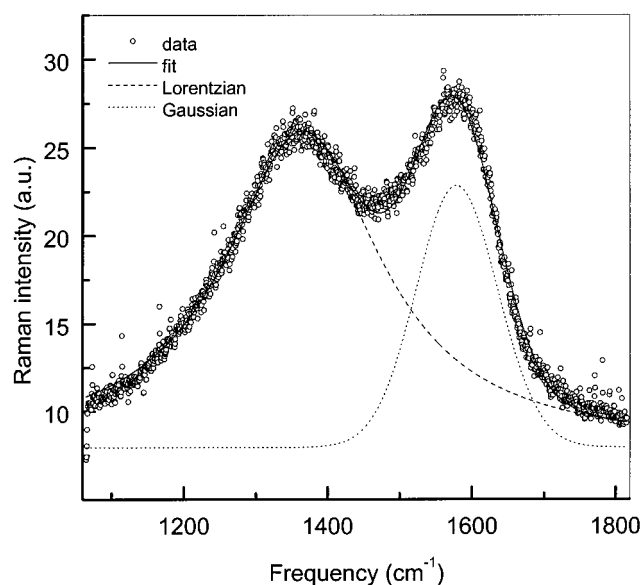


Figure 2. Micro-Raman spectrum of the second film: experimental data (○) and fit by Gaussian deconvolution (solid line).

Figure 2 shows the micro-Raman spectrum of the second sample in the region of 1200–1800 cm^{-1} . In the treatment of Raman spectra, line shapes were analyzed with a Lorentzian or Gaussian deconvolution. Two broad lines are seen at 1581 ± 2 and $1361 \pm 5 \text{ cm}^{-1}$ with widths of ~ 110 and $\sim 220 \text{ cm}^{-1}$,

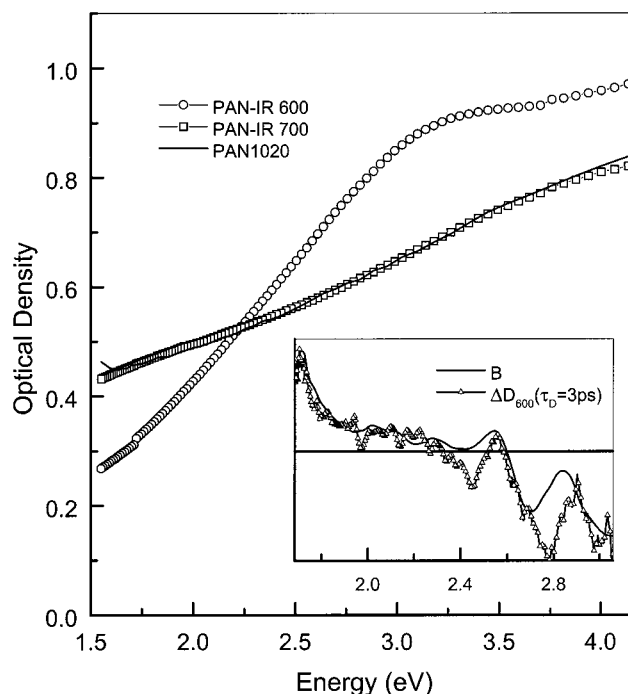


Figure 3. Stationary absorption spectrum of the first sample (○) and of the second sample (□). The spectrum of a PAN film¹⁴ carbonized at 1020 °C (solid line) is shown for comparison. In the inset, the second derivative of the optical density (solid line) and the photoinduced signal at time delay $\tau_D = 3 \text{ ps}$ (Δ) for the first sample are shown.

respectively. The ratio of the integral intensities of the line at 1361 cm^{-1} (I_D) to that at 1581 cm^{-1} (I_G), obtained from the Gaussian deconvolution, is ~ 1.9 . The Raman spectrum of the first-type film is similar to the second one, with the same peak position, but the ratio of the line intensities is ~ 3.4 . For pure graphite, the line at 1582 cm^{-1} corresponds to the Raman active mode E_{2g} .¹⁷ The line at 1357 cm^{-1} is attributed to the disorder-induced mode.¹⁸ This line does not appear in large grain single crystals but does appear in well-crystallized graphites with a small domain size.

The stationary absorption spectra $D(E)$ of the samples in the region from 1.5 to 4.1 eV are shown in Figure 3. Both spectra are structureless and show a slow increase in absorption when going to shorter wavelengths. We also calculated the first and second derivatives of the stationary spectra for both samples. While the first derivatives are qualitatively similar and featureless in the spectral region under study, the second derivatives differ significantly (for the first-type film the second derivative is shown in the inset of Figure 3).

From the absorption spectra^{14,16} of several PAN films that were pyrolyzed at temperatures from 245 to 1020 °C, it follows that the absorption coefficient $\alpha = 29 \pm 4 \text{ } \mu\text{m}^{-1}$ at $\hbar\omega \approx 4 \text{ eV}$ is nearly insensitive to the temperature of the heat treatment. This value was used to estimate the film thickness (see section 2).

The optical band gap E_g is evaluated as¹⁹

$$D(E) = \frac{A_1(E - E_g)^2}{E} + A_2 \quad (1)$$

assuming that the band edges are parabolic. Here, A_1 and A_2 are constants. It follows from this relation that $E_g \approx 0.65 \text{ eV}$ for our first-type film and $E_g \approx 0$ for the second-type film. The absence of an energy gap reflects strong cyclization of the

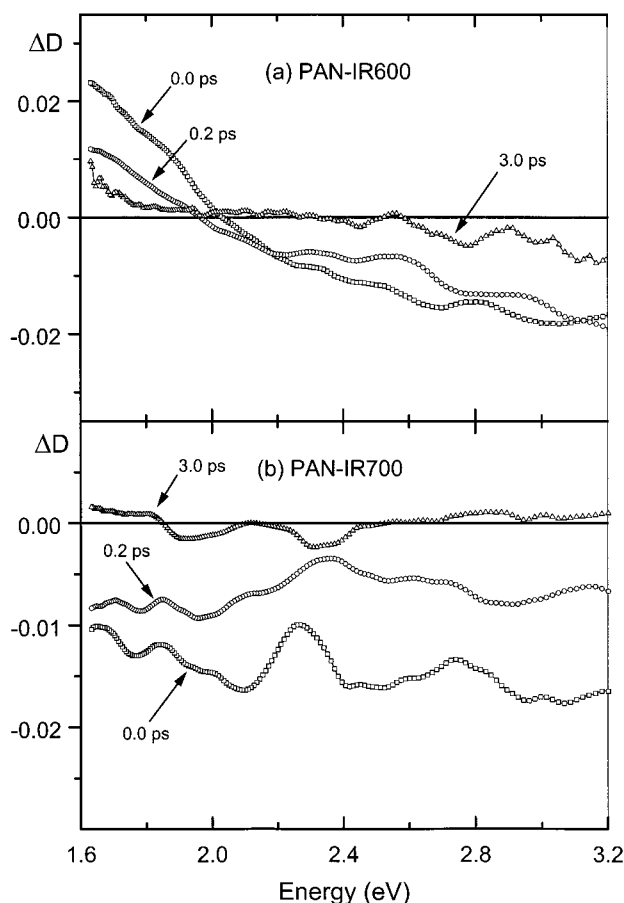


Figure 4. Photoinduced optical spectra of the first sample (a) and of the second sample (b) at different time delays. The spectra of the first sample were smoothed by triangular averaging over five energy points (~ 15 meV at $\hbar\omega \approx 2.4$ eV) and for the second sample over nine energy points. Symbols are shown for every ninth energy point.

polymer and creation of more extended graphite-like structures compared to the first sample.

3.2. Transient Spectra and Relaxation Rates. Transient photoinduced spectra $\Delta D(\omega)$ measured at different time delays τ_D are shown in Figure 4. For the first-type film, there is photoinduced darkening in the region 1.6–1.95 eV and photoinduced bleaching in the region 1.95–3.2 eV (Figure 4a). The zero crossing point shifts to higher energy with an increase of τ_D . Note the similarity of the photoinduced spectra $\Delta D(\omega)$ with the spectrum of the second derivative $D(\omega)''$. Both are positive for the energy region below 2 eV and negative for $\hbar\omega > 2.5$ eV. This similarity is most prominent for large time delays (see the inset in Figure 3). For the second-type film only photoinduced bleaching is observed at $\tau_D < 1$ ps over the whole energy region 1.6–3.2 eV (Figures 4b and 5).

The temporal dependence of the photoinduced spectra $\Delta D(\omega, t)$ has two time scales: fast, with a characteristic time of ~ 200 fs, and slow, with a characteristic time of a few picoseconds. Such a dependence is readily recognized for both samples from the kinetic traces $\Delta D(\omega, t)$ shown in Figure 5. The kinetic traces show a strong increase of the signal at early delays $\tau_D < 40$ fs, which is followed by two-stage relaxation. Note that the temporal behavior of the photoinduced optical density ΔD for the second-type film is in a good agreement with that of highly oriented pyrolytic graphite (HOPG) measured by a similar technique² for a pump fluence of 7.5 mJ/cm².

To obtain better understanding of the relaxation processes, we fitted the signal $\Delta D(\omega, t)$ with a biexponential function

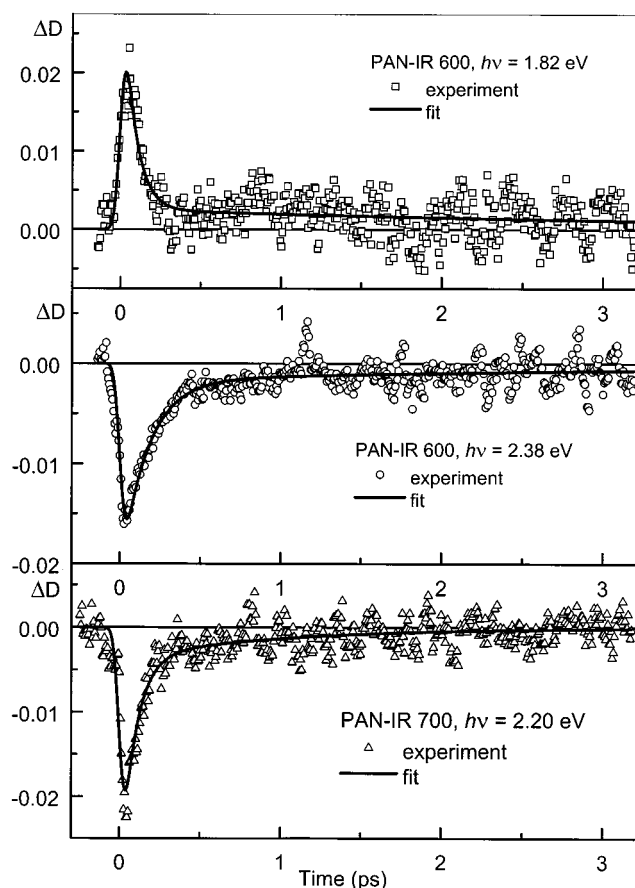


Figure 5. Kinetic traces of the photoinduced optical density $\Delta D(\omega, t)$ for the first sample (a, b) and for the second sample (c) at different probing energies.

$$F(t) = \theta(t-t_0)\{B_1 \exp(-\gamma_1(t-t_0)) + B_2 \exp(-\gamma_2(t-t_0))\} \quad (2)$$

convoluted with the pump–probe cross-correlation $S(t)$

$$\Delta D_{\text{fit}}(\omega, t) = \int_{-\infty}^{+\infty} dt' S(t-t') F(t') \quad (3)$$

Here $\theta(t)$ is the step function and $B_{1,2}$ are linear fitting parameters. For the cross-correlation we use $S(t) = 1/\cosh^2(1.763t/\tau_{\text{cc}})$ with $\tau_{\text{cc}} = 67$ fs. The relaxation rates $\gamma_1(\omega)$ and $\gamma_2(\omega)$ and the zero time delay $t_0(\omega)$ are varied to obtain the best approximation to the experimental signal $\Delta D(\omega, t)$.

We found that the relaxation rates γ_1 and γ_2 depend on the probe wavelength (see Figure 6, which shows $\gamma_1(\omega)$ for both samples). For the first-type film γ_1 increases with energy from $\gamma_1 \approx 6$ ps⁻¹ to $\gamma_1 \approx 17$ ps⁻¹ in the region of photoinduced darkening, $1.6 < \hbar\omega_{\text{probe}} < 1.9$ eV, while γ_1 decreases with energy from $\gamma_1 \approx 12$ ps⁻¹ to $\gamma_1 \approx 6$ ps⁻¹ in the region of photoinduced bleaching, $2.1 < \hbar\omega_{\text{probe}} < 3.2$ eV. For the second-type film, we observed only an increase of the ultrafast relaxation rate from $\gamma_1 \approx 4$ ps⁻¹ to $\gamma_1 \approx 14$ ps⁻¹ in the whole spectral region 1.6–3.2 eV. Note that for the second-type film, the spectral behavior of the ultrafast relaxation rate γ_1 is similar to that of HOPG obtained for close pumping intensities²⁰ (see Figure 6b). The second relaxation rate γ_2 is about 0.1–1 ps⁻¹ or slower for both types of films. The limited interval of the time delays (up to 3 ps) does not allow for the determination of γ_2 with a better accuracy. Therefore, its spectral dependence is not shown.

3.3. Fourier Spectra. Ultrashort pump pulses may impulsively excite coherent phonon oscillations,²¹ which modulate

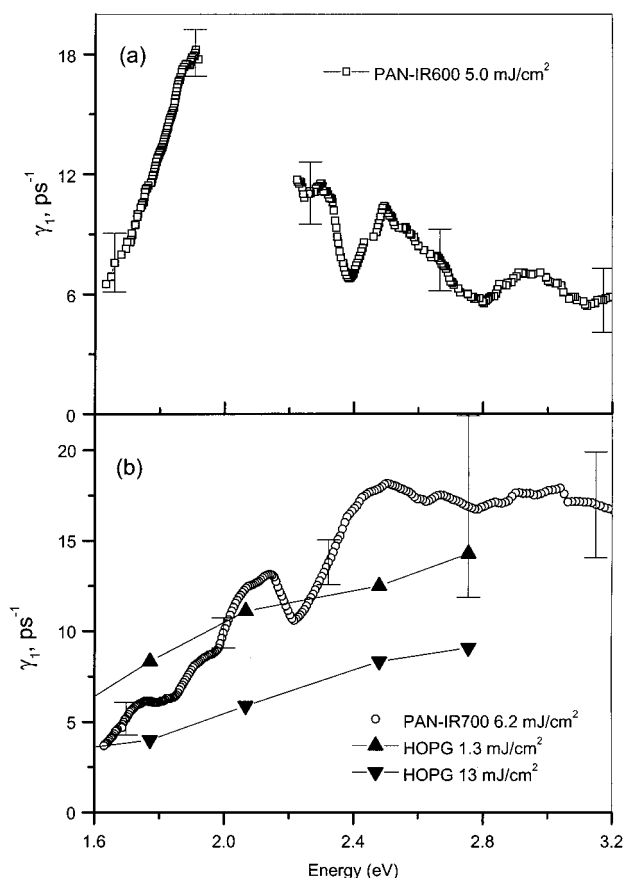


Figure 6. Spectral dependence of the ultrafast relaxation rate γ_1 for the first sample at a pump fluence of 5.0 mJ/cm² (a) and for the second sample at a pump fluence of 6.2 mJ/cm² (b). The transient signal for the first sample was very low in the probe energy region 2–2.1 eV; therefore, it is not shown. For comparison with the second sample, the HOPG relaxation rate²⁰ is shown in (b) for pump fluences of 1.3 (▲) and 13 mJ/cm² (▼).

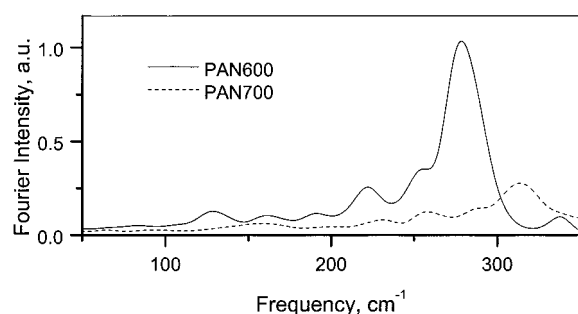


Figure 7. Fourier spectra of the oscillations observed in the first and second films.

the change of the dielectric function and thus vary the transmitted or reflected light intensity for time-delayed probe pulses. To determine the corresponding modulation frequencies, we first subtract the fitted kinetic traces $\Delta D_{\text{fit}}(\omega, t)$, given by eq 3, from their experimental counterparts $\Delta D_{\text{exp}}(\omega, t)$. From the Fourier transformation of the time-dependent differences, the spectra of coherent vibrations are obtained in the region 50–350 cm^{−1} with a resolution of 8 cm^{−1}. Coherent phonons were analyzed over the entire spectral range of the probing. A detailed description of this analysis has been reported elsewhere.²²

The analysis shows (see Figure 7) that for the first film there is a band at 280 cm^{−1} and for the second film there is no coherent vibration within our accuracy limits in the region from 50 to 350 cm^{−1}. A broad and saddle-shaped steady-state Raman

spectrum, with two maxima around 300 and 800 cm^{−1}, was observed in amorphous carbon films.^{14,23–25} This feature was considered to be characteristic for highly disordered a-C materials, being highly sensitive to short-range order.²⁵ It has been also found that this spectral feature becomes less pronounced and shifts toward higher frequency with an increase of annealing temperature.²⁵ From this we conclude that the first sample is much more disordered than the second.

4. Discussion

4.1. Film Structure. The sample structure can be derived from its Raman spectra. The Raman spectra of the second-type film shown in Figure 2 are similar to those of PAN films carbonized at 1020–1220 °C.¹⁴ Usually in graphite structures, the position of the E_{2g} mode varies in the range 1580–1592 cm^{−1}; the lower this frequency, the more perfect is the local structure.¹⁷ The line broadening, especially for the E_{2g} mode, is related to disorder within a carbon sheet.²⁶ From our data, it follows that both samples are rather disordered materials despite the small deviations in the bond angles and bond lengths from those of graphite.

The average size L_a of the graphite-like clusters can be estimated from the empirical relation^{18,26}

$$L_a = 44(I_D/I_G)^{-1} [\text{\AA}] \quad (4)$$

which connects L_a with the Raman line integral intensities ratio I_D/I_G . Equation 4 gives the average size of the graphite-like domain of 13 and 23 Å for the first- and second-type film, respectively. Such a small crystalline domain size is consistent with literature data^{14,27} on other carbon films. (Note that for such small crystallites the intensity ratio (eq 4) is not very sensitive to the size and can be used to obtain a rough estimation only.)

The stationary absorption spectrum of the first-type film (Figure 3) is typical for PAN films obtained at a lower stage of pyrolysis.^{12,14,16} For the second-type film the absorption coefficient is smaller at ~3 eV and larger below 2 eV compared to that of the first sample. A smaller optical density in the region of 4 eV for the second sample results from its smaller thickness (see section 3.1) due to the higher temperature of treatment.

As seen from Figure 3, the linear optical spectrum of the second-type film (squares) is similar to that of a PAN film carbonized at 1020 °C by traditional pyrolysis (solid line).¹⁴ Both spectra coincide in the entire energy region except the low-energy part, <1.65 eV, where the optical density of the PAN (1020 °C) film increases with lowering of the energy. The similarity of the linear optical density and Raman spectra of the second-type film to those of PAN (1020 °C)¹⁴ indicates the similarity in atomic ordering and points to an electronic structure that is close to that of microcrystalline graphite. In ref 14 the crystalline domain size was determined to be 20 Å from electron diffraction and dark-field transmission microscopy. Note that the optical spectrum for the second-type film is also similar to that of the glassy carbon.²⁸

An average size of crystallites can be also estimated from optical spectra using the energy gap dependence

$$E_g \approx 2|\beta|M^{-0.5} \quad (5)$$

on the number M of 6-fold rings in compact carbon clusters.⁴ It follows from this relation (with $\beta = -2.5$ eV) that the first sample has an average crystalline size of ≤ 17 Å. This estimate agrees well with that derived from eq 4. The absence of an

energy gap for the second-type film, as seen from the linear optical spectra, indicates that the second-type film has the larger average size of crystalline domains (and hence a more extended system of π bonds) than the first sample.

A measure of the ordering in a-C can be derived from its low-frequency vibrational spectrum.²⁵ Here, one could expect the disorder-induced appearance of the graphite (TA_\perp , TO_\perp) mode. The intensity of this mode and its frequency shift from the M -point value (of 466 cm^{-1})²⁹ should be proportional to $1/L_a$. Using the experimental phonon dispersion curves²⁹ for pyrolytic graphite and the value of 280 cm^{-1} for the vibrational band, we estimate the average size of graphitic clusters as $\sim 14 \text{ \AA}$ for the first sample. The absence of oscillations in the spectral range $h\nu < 350 \text{ cm}^{-1}$ for the second sample indicates that the average size of graphitic cluster is $> 18 \text{ \AA}$. This is also in agreement with the estimates obtained above by other methods.

The quality of the film surfaces can be judged from the AFM images. As directly seen from Figure 1, the second-type film has a significantly larger average size of cluster aggregates compared to the first one. This suggests an increase of the average size of the cluster itself and a significantly higher long-range order. This is also supported by the absence of pores in the second-type sample.

4.2. Photoinduced Spectra. From the analysis of transient spectra $\Delta D(t, \omega)$ shown in Figure 4, we find that for the first-type film the spectra can be decomposed into two contributions

$$\Delta D(t, \omega) = \Delta D_1(t, \omega) + \Delta D_{\text{sf}}(t, \omega) \quad (6)$$

The first term $\Delta D_1(t, \omega) = C_1(t) D''(\omega)$ is proportional to the second derivative of the optical absorption $D(\omega)$, and the second term is due to bleaching that results from the band states filling $\Delta D_{\text{sf}}(t, \omega) = [dD(\epsilon)/d\epsilon] \Delta \epsilon_{\text{sf}}(t, \omega)$. Here, $\epsilon = \epsilon_1 + i\epsilon_2$ is the dielectric function of the sample and $\Delta \epsilon_{\text{sf}}(t, \omega)$ is its change due to states-filling. From the dielectric function^{14,16,28} for different types of amorphous carbon and for graphite, it follows that in the spectral region under study $dD/d\epsilon_1 \ll dD/d\epsilon_2$. Therefore, we consider the difference in optical density to be mainly determined by a change of the imaginary part of the dielectric function $\Delta D(\omega, t) \propto \Delta \epsilon_2(\omega, t)$.

It follows from calculations that at early pump–probe delays, the two contributions ΔD_1 and ΔD_{sf} are of the same order of magnitude and they have opposite signs in the probe energy region from 2 to 2.4 eV. With increasing pump–probe delay, ΔD_{sf} vanishes more quickly than ΔD_1 . This is seen in the transient spectra of Figure 4 as a temporal shift of the zero crossing point to higher probe energies. At longer delays, the photoinduced spectra can be approximated by the first contribution solely as $\Delta D(t, \omega) \approx C_1(t) D''(\omega)$ as is shown by the inset in Figure 3.

A reason for the observation of the $\Delta D_1(t, \omega)$ contribution may be a random local electric field $\Delta \mathbf{E}_i$ created by charge-transfer transitions. This results in an absorption change

$$\Delta D_1(E) \approx \frac{\partial^2 D(E)}{\partial E^2} (\Delta \mathbf{E}_i)^2 \quad (7)$$

These random local electric fields appear because free charge carriers are created by photon absorption. However, an electron and hole cannot be separated by a large distance, since the mean free path must be on the order of or less than the crystalline domain size, which is 10 \AA . Therefore, random electric fields appear in the first-type films at very early delays. For longer

time, the energy relaxation of the carriers leads to the localization of carriers on trapping centers, thus freezing out the random electric field.

For the second sample, the photoinduced spectra at zero delay can be represented by the states-filling contribution only, $\Delta D(t, \omega) \approx \Delta D_{\text{sf}}(t, \omega)$. Such a difference, compared to the first film, can be understood by assuming the ΔD_1 contribution to be inversely proportional to the size of graphite-like clusters. Then for the second-type film, this contribution is suppressed and is mainly defined by the presence of small size clusters. Additionally, for the second-type film, there is a higher density of states in the vicinity of the Fermi level³ and a much broader distribution of nonequilibrium carriers is created during pump pulse absorption.

4.3. Relaxation Rates. For amorphous carbon films, a similarity between the optical properties of aromatic hydrocarbons and graphite is expected. The larger the average size of the graphite-like sheets, the closer are the optical properties to those of graphite. Therefore, let us consider the spectral dependence of the relaxation rate in graphite and graphite-like materials.

The main effect of optical pumping in graphite is the filling of the band states by hot carriers.²⁰ The absorption of photons results in the promotion of electrons from the valence band to the conduction band, thus creating a population difference between the excited and ground states. The nonequilibrium distribution of carriers in the conduction and valence bands thermalizes rapidly because of the electron–electron and electron–plasmon scattering. This fastest stage of quasiparticle relaxation in graphite was studied both experimentally³⁰ and theoretically.³¹ It was shown that for quasiparticles with energy $E - E_F > 0.8 \text{ eV}$ the electron–electron relaxation rate γ_{e-e} is greater than $1/40 \text{ fs}^{-1}$. This relaxation rate increases linearly with energy for a wide energy region, $E - E_F > 0.3 \text{ eV}$, as $\gamma_{e-e}(E) = C(E - E_F)$ with $C = 29 (49) \text{ eV}^{-1} \text{ ps}^{-1}$ according to ref 30 (31). This process leads to a high-temperature, quasi-Fermi distribution of carriers in the bands (with carrier temperature T_e up to $\sim 1 \text{ eV}$ for pumping at $\hbar\omega_{\text{pu}} = 2.34 \text{ eV}$), which in turn causes a decrease of absorption over a wide spectral range. However, the time resolution in our experiment is not sufficient to monitor this earlier stage of relaxation.

The subsequent evolution of the system will be governed by the electron–phonon interaction. The hot electrons and holes transfer their energy to the lattice and relax toward the respective band extrema. The evolution of the electron temperature at this stage can be described by the equation

$$\frac{\partial T_e}{\partial t} = -\gamma_T (T_e - T_L) \quad (8)$$

where γ_T is the electron temperature relaxation rate coefficient, which can be a function of time.³²

The change of $\epsilon_2(\omega, t)$ in the probe energy region 1.8–3.2 eV comes mainly from interband ($i = \pi$) \rightarrow ($f = \pi^*$) transitions and can be expressed as

$$-\Delta \epsilon_2(\omega, t) = \frac{4\pi^2 e^2 \hbar^2}{3m^2 \omega^2} \int \frac{2}{(2\pi)^3} d\vec{k} |P_{fi}(\vec{k})|^2 [n(E_f(\vec{k})) + n(-E_i(\vec{k}))] \delta(E_f(\vec{k}) - E_i(\vec{k}) - \hbar\omega) \quad (9)$$

Here, P_{fi} is the matrix element of the momentum and $n(E_i)$ is the electron energy distribution function in the π band. The electronic structure of a single graphite layer and of compact clusters of fused 6-fold carbon rings is symmetric about $E = 0$.

This symmetry property approximately holds for graphite and amorphous carbons.^{3,4} Therefore, we can write

$$-\Delta\epsilon_2(\omega, t) = \frac{8\pi^2 e^2 \hbar^2}{3m^2 \omega^2} \left| P_{\text{fi}} \left(\sqrt{\frac{2m_{\text{fi}}}{\hbar^2}} (\hbar\omega - E_g) \right) \right|^2 J_{\text{fi}}(\hbar\omega) n \left(\frac{\hbar\omega - E_g - 2\mu_f}{2T_e} \right) \quad (10)$$

Here, $J_{\text{fi}}(\hbar\omega)$ is the reduced density of states for the $\pi \rightarrow \pi^*$ interband transition

$$J_{\text{fi}}(\hbar\omega) = \int \frac{2}{(2\pi)^3} d\vec{k} \delta(E_f(\vec{k}) - E_i(\vec{k}) - \hbar\omega) \quad (11)$$

The relaxation rate of the dielectric function can be found from

$$\gamma_{\text{e-ph}} = -\frac{\partial}{\partial t} \log[-\Delta\epsilon_2(\omega, t)] = \left[1 - n \left(\frac{\hbar\omega - E_g - 2\mu_f}{2T_e} \right) \right] [a + b\hbar\omega] \quad (12)$$

where

$$a = -\frac{\partial}{\partial t} \left(\frac{E_g + 2\mu_f}{2T_e} \right), \quad b = -\frac{1}{2T_e} \frac{\partial \log T_e}{\partial t} \approx \frac{\gamma_T}{2T_e} \quad (13)$$

Taking into account that for graphite $E_g \approx 0$ and noting that for the spectral region under consideration $(\hbar\omega - 2\mu_f)/(2T_e) > 1$, we obtain a linear energy dependence for $\gamma_{\text{e-ph}}$:

$$\gamma_{\text{e-ph}}(\hbar\omega) \approx a + b\hbar\omega \quad (14)$$

As is seen from Figure 6, the spectral dependence of the relaxation rate for the film of the first type differs significantly from that of the second type. For the first film γ_1 has a nonmonotonic spectral dependence with a maximum around 2 eV. The spectral behavior of γ_1 for the second film is nearly linear and similar to that of HOPG,²⁰ measured in the same range of pumping intensities. This indicates that the increase of the temperature of heat treatment from 600 to 700 °C leads to substantial carbonization of the sample, i.e., to the appearance of percolating graphite-like clusters. This conclusion is in agreement with the estimates of the average cluster size from Raman, stationary optical, and Fourier spectra discussed above.

In deriving eq 14, we make use of $E_g = 0$ and the symmetry of the energy band structure relative to $E = 0$. The symmetry property is valid for aromatic clusters and approximately pertains to amorphous carbons.³ It follows from eq 12 that with $E_g \neq 0$ there is no maximum in the spectral dependence of $\gamma_{\text{e-ph}}$. Therefore, the specific dependence of the relaxation rate for the first film originates from another mechanism, which is different from the electron–phonon interaction.

4.4. Two Types of Optical Transitions. We believe that the above-mentioned differences between the first- and second-type film result from a smaller carbon cluster size L_a for the first sample ($L_a \approx 13$ Å) compared to the second sample. The first film can be considered as a molecular solid composed of planar molecules, carbon clusters with nitrogen on the boundaries. We suggest two types of π – π^* optical transitions in such systems: usual intramolecular transitions when the excited electron stays within the same cluster and intermolecular charge-transfer transitions. Intermolecular transitions result in a charge separation between nearby clusters; this creates a local electric field that distorts the clusters and leads to a splitting of the molecular

levels and, hence, to broadening of the joint density of states. The resulting photoinduced response is described by eq 7 and is similar to that observed in C₆₀ molecular crystals.^{22,33}

With increasing cluster size, the local electric field and its effect on the density-of-states broadening decrease, and hence, only intramolecular transitions finally survive as it takes place in graphite. The importance of charge-transfer transitions was also pointed out for the interpretation of the photoinduced spectra of a conjugated polymer polyaniline (in the form of emeraldine base).³⁴ Intramolecular transitions are also cluster-size-dependent, but this dependence should be rather smooth for a cluster size larger than 15 Å.

We suggest that the absence of photoinduced absorption in the second film is a consequence of more extended graphite-like domains, so the contribution of charge transfer (intermolecular) transitions to the photoinduced response is, first, suppressed and, second, shifted to lower energies. The main contribution to the signal comes then from heating of charged carriers and their subsequent energy relaxation. The behavior of the optical response for the energy region far from the Fermi level must then be similar to that of graphite, as indeed it is for the second sample. The broadband absorption saturation caused by state filling by a hot π band electron population was experimentally observed for HOPG.²⁰

5. Conclusion

We studied the photoinduced response of new carbon PAN-IR films over the spectral range 1.6–3.2 eV with 40 fs time resolution. The study reveals an ultrafast component of the photoinduced signal with a time constant less than 100 fs. An increase of the effective temperature of the heat treatment leads to a corresponding increase of the average size of the crystalline domain, which changes the electronic structure and relaxational properties of carbon films.

The relaxation rates γ_1 and γ_2 were found to depend on probe wavelength. For the first-type film, γ_1 increases from 6 to 17 ps^{−1} in the probe region, $1.6 < \hbar\omega_{\text{probe}} < 1.9$ eV, while γ_1 decreases from 12 to 6 ps^{−1} in the region $2.1 < \hbar\omega_{\text{probe}} < 3.2$ eV. For the second film we observed a monotonic increase of the ultrafast relaxation rate, from 4 to 14 ps^{−1}, in the range 1.6–3.2 eV. For the film with small graphite-like domains of 13 Å (first sample), we propose two types of optical transitions that contribute to the photoinduced transient spectra. The first is the ordinary intramolecular absorption when photoexcited electrons stay within the same cluster. The second type is the intermolecular charge-transfer transition, when the photoexcited electron is transferred from one cluster to another close one. For large size clusters, the contribution of these intermolecular transitions is diminished, so only intramolecular excitations survive.

Acknowledgment. We thank N.P. Ernstring for helpful discussions. The work was supported by a grant from Deutschen Forschungsgemeinschaft (DFG) and in part by grants from International Science and Technology Center (Grant 872) and from Russian Foundation of Basic Research. V.M.F. thanks A. L. Dobryakov for his help in the early stages of this work.

References and Notes

- (1) Noda, T.; Inagaki, M.; Yamada, S. *J. Non-Cryst. Solids* **1969**, *1*, 285.
- (2) Jenkins, G. M.; Kawamura, K.; Ban, L. L. *Proc. R. Soc. London* **1972**, *A327*, 501.
- (3) Robertson, J. *Adv. Phys.* **1986**, *35*, 317.

- (4) Robertson, J.; O'Reilly, E. P. *Phys. Rev.* **1987**, *B35*, 2946.
- (5) Angus, J. C.; Wang, Y.; Sankara, M. *Annu. Rev. Mater. Sci.* **1991**, *21*, 221.
- (6) McKenzie, D. R. *Rep. Prog. Phys.* **1996**, *59*, 1611.
- (7) Raman, V.; Coffey, K. R. *Appl. Phys. Lett.* **1991**, *59*, 25.
- (8) Matsubara, H.; Yamaguchi, Y.; Shioya, J.; Murakami, S. *Synth. Met.* **1987**, *18*, 503.
- (9) Angus, J. C.; Hayman, C. C. *Science* **1988**, *241*, 913.
- (10) Schueller, O. J. A.; Brittain, S. T.; Whitesides, G. M. *Adv. Mater.* **1997**, *9*, 477.
- (11) Zaloznaya, N. F.; Zemtsov, L. M.; Karpacheva, G. P.; Davydov, B. E.; Kozlov, Yu. G.; Shchekin, I. A.; Khrekin, A. V. *USSR Inventors Certificate N 1721634 Byul. Izobr.* **1992**, *N11*.
- (12) Zemtsov, L. M.; Karpacheva, G. P. *Polym. Sci.* **1994**, *A36*, 758.
- (13) Shul'ga, Yu. M.; Rubtsov, V. I.; Efimov, O. N.; Karpacheva, G. P.; Zemtsov, L. M.; Kozlov, V. V. *Polym. Sci.* **1996**, *A38*, 636.
- (14) Renschler, C. L.; Sylwester, A. P. *Appl. Phys. Lett.* **1987**, *50*, 1420.
- Renschler, C. L.; Sylvester, A. P.; Salgado, L. V. *J. Mater. Res.* **1989**, *4*, 452.
- (15) Kovalenko, S. A.; Dobryakov, A. L.; Ruthmann, J.; Ernsting, N. P. *Phys. Rev.* **1999**, *A59*, 2369. Kovalenko, S. A.; Ernsting, N. P.; Ruthmann, J. *Chem. Phys. Lett.* **1996**, *258*, 445.
- (16) Chung, T. C.; Schlesinger, Y.; Etemad, S.; Macdiarmid, A. G.; Heeger, A. J. *J. Polym. Sci.* **1984**, *22*, 1239.
- (17) Dresselhauss, M. S.; Dresselhaus, G. In *Light Scattering in Solids*; Cardona, M., Güntherodt, G., Eds.; Springer: Berlin, 1982; Vol. III, p 3.
- (18) Tuinstra, F.; Koenig, J. L. *J. Chem. Phys.* **1970**, *53*, 1126.
- (19) Tauc, J.; Grigirovici, R.; Vancu, A. *Phys. Status Solidi* **1966**, *15*, 627.
- (20) Seibert, K.; Cho, G. C.; Kütt, W.; Kurz, H.; Reitze, D. H.; Dadap, J. I.; Ahn, H.; Downer, M. C.; Malvezzi, A. M. *Phys. Rev.* **1990**, *B42*, 2842.
- (21) Merlin, R. *Solid State Commun.* **1997**, *102*, 207.
- (22) Farztdinov, V. M.; Dobryakov, A. L.; Letokhov, V. S.; Lozovik, Yu. E.; Matveets, Yu. A.; Kovalenko, S. A.; Ernsting, N. P. *Phys. Rev.* **1997**, *B56*, 4176.
- (23) Smith, J. E., Jr.; Brodsky, M. H.; Crowder, B. L.; Nathan, M. I. *J. Non-Cryst. Solids* **1972**, *8-10*, 179.
- (24) Wada, N.; Gasci, P. J.; Solin, S. A. *J. Non-Cryst. Solids* **1980**, *35&36*, 543.
- (25) Wang, Q.; Allred, D. D.; Gonzales-Hernandez, J. *Phys. Rev.* **1993**, *B47*, 6119.
- (26) Knight, D. S.; White, W. B. *J. Mater. Res.* **1989**, *4*, 385.
- (27) Rouzand, J. N.; Oberlin, A.; Beny-Bassley, C. *Thin Solid Films* **1983**, *105*, 75.
- (28) Arakawa, E. T.; Williams, M. W.; Inagaki, T. *J. Appl. Phys.* **1977**, *48*, 3176.
- (29) Nicklow, R. M.; Wakabayashi, N.; Smith, H. G. *Phys. Rev.* **1972**, *B5*, 4951.
- (30) Xu, S.; Cao, J.; Miller, C. C.; Mantell, D. A.; Miller, R. J. D.; Gao, Y. *Phys. Rev. Lett.* **1996**, *76*, 483.
- (31) Gonzales, J.; Guinea, F.; Vozmediano, M. A. H. *Phys. Rev. Lett.* **1996**, *77*, 3589.
- (32) Allen, P. B. *Phys. Rev. Lett.* **1987**, *59*, 1460.
- (33) Farztdinov, V. M.; Kovalenko, S. A.; Matveets, Yu. A.; Starodubtsev, N. F.; Marowsky, G. *Appl. Phys.* **1998**, *B66*, 225.
- (34) Misurkin, I. A.; Zhuravleva, T. S.; Geskin, V. M.; et al. *Phys. Rev.* **1994**, *B49*, 7178.